

Local structure determination of Zn-smectite

QI TAO^{1,2,*}, CHAOGANG XING³, SEUNGYEOL LEE^{4,5}, LONG YANG^{6,7}, QINGJIN ZENG^{1,8},
SHANGYING LI^{1,†}, TIANQI ZHANG^{1,8}, GUANGLIE LV³, HONGPING HE^{1,2}, AND SRIDHAR KOMARNENI^{9,*}

¹CAS Key Laboratory of Mineralogy and Metallogeny and Guangdong Provincial Key Laboratory of Mineral Physics and Materials, Guangzhou Institute of Geochemistry, Chinese Academy of Sciences, Guangzhou, 510640, P.R. China

²CAS Center for Excellence in Deep Earth Science, Guangzhou, 510640, P.R. China

³Analysis Center of Agrobiolgy and Environmental Sciences of Zhejiang University, Hangzhou, 310058, P.R. China

⁴USRA Lunar and Planetary Institute, 3600 Bay Area Boulevard, Houston, Texas 77058, U.S.A.

⁵Department of Earth and Environmental Sciences, Chungbuk National University, Cheongju 28644, Republic of Korea

⁶Department of Applied Physics and Applied Mathematics, Columbia University, New York, New York 10027, U.S.A.

⁷School of Materials Science and Engineering, Tongji University, Shanghai 201804, P.R. China

⁸University of Chinese Academy of Sciences, Beijing 100049, P.R. China,

⁹Department of Ecosystem Science and Management and Materials Research Institute, 204 Energy and the Environment Laboratory, The Pennsylvania State University, University Park, Pennsylvania 16802, U.S.A.

ABSTRACT

An aluminum-free zinc-bearing smectite (Zn-smectite) was synthesized under hydrothermal conditions, together with its magnesium substituted products. Its layer charge calculated by cation exchange capacity (CEC) is 117.4 mmol/100 g. Powder X-ray diffraction (XRD) revealed turbostratic stacking and showed that the d_{061} value of the Zn-smectite was >1.525 Å, indicating that it is trioctahedral. Its d_{001} value increased from ca. 12.8 Å to ca. 16.0 Å after ethylene glycol (EG) saturation. The Zn-smectite did not irreversibly collapse after heating the Li⁺-saturated sample to 300 °C, suggesting that its layer charge was generated from octahedral-site vacancies (defects). The Zn-smectite resembles zinsilite-like minerals with interlayer Na⁺ and Zn²⁺. The intralayer structure of zinsilite was confirmed by pair distribution function (PDF) analysis, and the whole crystal structure was built and optimized by DFT calculation in the CASTEP module of the Materials Studio software. Synthetic zinsilite is triclinic, space group $P\bar{1}$, and its optimized unit-cell parameters are: $a = 5.294$ Å, $b = 9.162$ Å, $c = 12.800$ Å, $\alpha = 90.788^\circ$, $\beta = 98.345^\circ$, and $\gamma = 90.399^\circ$.

Keywords: Smectite, layer charge, local structure, turbostratic disorder, PDF

INTRODUCTION

Smectites are the most abundant group of clay minerals in Earth's near-surface environments, and they therefore, play crucial roles in geological processes, such as enrichment and migration of surface elements. Most smectites in soils and sediments are formed by weathering transformation of micas to vermiculites to smectites and by diagenetic and hydrothermal alteration of rocks (Hillier 2003). Zinc-rich smectites (Zn-smectites) are associated with supergene non-sulfide ores worldwide (Mondillo et al. 2015). Some of these are predominant economic minerals (e.g., saucanite) (Schingaro et al. 2021) of the mineral assemblage derived by weathering (Newman and Brown 1987; Ross 1946). As natural two-dimensional (2D) inorganic materials, Zn-smectites have wide applications as catalysts and catalyst supports, luminescent materials, adsorbents, etc. (Liu and Zhang 2014; Wang et al. 2019).

Zinsilite is a Zn-containing but aluminum-free end-member of the montmorillonite-zinsilite series (Smolianinova et al. 1960), whose crystal structure is far from well understood (Bergaya and Lagaly 2013). At present, there are relatively few

studies on Zn-smectites synthesis (Ponce and Klopogge 2020; Vogels et al. 2005; Zhou et al. 2017) compared with saponite and hectorite of the same subgroup (Klopogge et al. 1999). These studies were conducted mainly on synthetic Zn-smectites prepared in the presence of Al (Ponce and Klopogge 2020; Vogels et al. 2005; Zhou et al. 2017). There had been no recording of the synthesis of such a mineral until 2008 (Petit et al. 2008), although they considered their products to be saucanite-like stevensite. The products were proposed to have a similar structural formulas with stevensite, but with octahedral Zn instead of Mg, i.e., $R_x^+Si_4(Zn_{3-x}\square_x)O_{10}(OH)_2$, where R⁺ and x are for interlayer cations and the number of octahedral vacancies, respectively (Petit et al. 2008). Apart from the results of Petit et al. (2008), no reliable unit-cell parameters and structural information are available for smectites of this series (Anthony et al. 2001). A lack of crystal structure information of these smectites would limit their potential applications, for example, affecting the revelation of the reaction mechanism when they are used as functional materials.

Refining the crystal structure of smectites is difficult, primarily because they lack three-dimensional (3D) order structures and because of their fine grain size (usually <2 μm) and widespread layer stacking disorder (such as rotation and translational shifts) (Meunier 2006). Random rotations and translations within the

* E-mail: taoqi@gig.ac.cn. Orcid 0000-0003-3041-7299. E-mail: sxk7@psu.edu
† Orcid 0000-0002-1900-5077

a-b plane produce turbostratically disordered structures (Brindley and Brown 1980; Moore and Reynolds 1997; Ufer et al. 2004). In such cases, adjacent layers are no longer optically coherent with each other, and no orientation of the crystal can produce *hk0* (or *hkl*) reflections from more than one layer (Brindley and Brown 1980; Moore and Reynolds 1997). For crystals containing successive turbostratic stacking layers, asymmetric *hkl* reflections were obtained, as a characteristic of 2D crystals, similar to those from a single layer (Lanson et al. 2011; Ufer et al. 2004). These types of disorder make the common models insufficient to simulate the XRD profiles simply by broadening Bragg reflections and the traditional Rietveld refinement completely inappropriate to the structural determination and quantitative analysis of smectites (Ufer et al. 2004).

Computer programs were built to model the disordered layer structures of 2D materials, such as DIFFaX (Braunbarth et al. 2000; Hines et al. 1997; Treacy et al. 1991), DIFFaX+ (Leoni et al. 2004), FAULTS (Casas-Cabanas et al. 2016), ROSS-X (Leonardi and Bish 2020), etc. These programs have been used to model diffraction from phyllosilicates, such as talc, kaolinites, illite, etc., but have not for smectites (Artoli et al. 1995; Gualtieri 1999; Gualtieri et al. 2008; Viani et al. 2002). It was until 2004 that Ufer et al. (2004, 2008) proposed a method (Ufer single model) based upon the Debye formula (Debye 1915; Yang and Frindt 1996) for modeling diffraction effects from smectites with turbostratic disorder within the Rietveld method. Their models combined periodic/pseudoaperiodic calculations, providing a successful and fast method for XRD profile simulation and phase quantifications of smectites, as included in the BGMN program (Ufer et al. 2004, 2008, 2012). With further development, structural features, such as layer charge density and occupancies of octahedral sites of dioctahedral smectite have been achieved using this method (Wang et al. 2018). Although in the above cases, models with special layer faults (such as those used in DIFFaX+) or super-cell (such as those in single layer method) were used to successfully simulate XRD patterns of smectites, the crystal structure of smectite based on these simulation results is still lacking, especially for the relevant atomic coordinates.

The atomic pair distribution function (PDF) method is a total scattering technique, which gives the scaled probability $G(r)$ of finding two atoms in a material at a distance r apart (Egami and Billinge 2012; Neder and Proffen 2008; Young and Goodwin 2011). It uses both the Bragg reflections and the diffuse scattering (Lee and Xu 2020). Therefore, it can be used to investigate not only the long-range ordered structure, but also the short-range ordered local structure of a solid, such as poorly ordered phases (e.g., nanocrystals and gels) and amorphous phases (e.g., glasses and liquids) (Young and Goodwin 2011; Juhás et al. 2010; Ojovan and Louzguine-Luzgin 2020; Schlesinger et al. 2021). PDF analysis can reveal the atomic structure from the total scattering data using the real-space refinement method (Billinge and Kanatzidis 2004; Lee and Xu 2020). It is therefore a promising technique to determine the local structure of smectite.

In the present study, aluminum-free zinc-bearing smectite (Zn-smectite) and its magnesium-substituted products (with varying molar ratios of octahedral Zn^{2+}/Mg^{2+} cations) were synthesized under hydrothermal conditions. The obtained

samples were characterized by XRD, ^{29}Si solid-state magic-angle spinning nuclear magnetic resonance spectroscopy (^{29}Si MAS NMR), and transmission electron microscopy (TEM). Their layer charges were determined from their cation exchange capacities (CECs). Based on PDF analysis and refinement of selected structural models, the intralayer structure of Zn-smectite was obtained using PDFgui program (Farrow et al. 2007). Subsequently, the overall structure of Zn-smectite (including H in hydroxyl group and interlayer cations) was constructed by Materials Studio software and optimized by DFT calculations. This is the first case to study the local structure of Zn-smectite and build its crystal structure with turbostratically disordered layers based on PDF analysis.

SAMPLES AND METHODS

Hydrothermal experiments

The synthesis of Zn-smectites used 10.23 g (0.036 mol) $Na_2SiO_3 \cdot 9H_2O$ ($\geq 98.0\%$, Aladdin) and desired amounts of $ZnCl_2$ ($\geq 98.0\%$, Guangzhou Chemical Reagent Factory) and $MgCl_2 \cdot 6H_2O$ (98.0%, Guangzhou Chemical Reagent Factory), which were dissolved in 25 mL deionized (DI) water. 4.00 mol L^{-1} NaOH ($\geq 96.0\%$, Guangzhou Chemical Reagent Factory) solution was added to the above mixture while stirring until its pH reached ca. 10.00, which was maintained for half an hour, and after the equilibration a uniform gel was eventually obtained. The total volume of the mixtures was kept at 75 mL by adding DI water. After that, the gel was transferred to a 100 mL polytetrafluoroethylene-lined stainless steel autoclave and treated at 180 °C for 48 h. The obtained precipitates were washed by several centrifuge–washing cycles until the supernatant reached neutral pH followed by drying at 65 °C and grinding for further treatments. The amounts of $ZnCl_2$ and $MgCl_2 \cdot 6H_2O$ were calculated by fixing the mole ratio of Si/M^{2+} as 3:2 per half unit cell (p.h.u.c.) $[O_{10}(OH)_2]$, in which M^{2+} represents the sum of the amounts of Zn^{2+} and Mg^{2+} (in moles). This ratio was intentionally set to ensure that the Si amount was sufficient for the formation of a trioctahedral smectite structure ($Si/M^{2+} = 4:3$). The obtained products were marked as S-Zn $_x$ ($x = 1, 2, 3$ and 4). For example, S-Zn1 represents the sample synthesized with 6 mol of Si, 1 mol of Zn, and 3 mol of Mg in the starting chemicals.

The CECs of the synthesized samples were determined using the $[Co(NH_3)_6]^{3+}$ method (Bisio et al. 2008). Briefly, a mixture of 500 mg synthetic samples and 30 mL 50 mmol L^{-1} $[Co(NH_3)_6]Cl$ ($>99.0\%$, Aladdin) solution was shaken by a shaking table at room temperature for 24 h to thoroughly exchange cations on the surfaces and in the interlayers. After separation by centrifugation, the solution was analyzed by UV-Vis spectrophotometry (UV-7504). The decrease in absorbance at 474 nm, typical of the CT transition of $[Co(NH_3)_6]^{3+}$, was quantitatively related to the difference in concentration by means of calibration with standard solutions. The samples after $[Co(NH_3)_6]^{3+}$ exchange were designated as S-Zn $_x$ Co.

The Hofmann-Klemmen tests were done using the method described in the literature (Petit et al. 2008). Typically, 250 mg S-Zn $_x$ Co was put into a 50 mL centrifuge tube with 30 mL 2.00 mol L^{-1} LiCl ($\geq 97.0\%$, Sinopharm Chemical Reagent) solution. After sealing, the tube was shaken to thoroughly mix the solid and solution using a shaking table for 2 h. After centrifugation, the supernatant solution was removed, and the samples were shaken with another 30 mL 2.00 mol L^{-1} LiCl solution for another 2 h. These treatments were repeated twice, and the mixing time was extended to 24 h. After drying at 75 °C, the products (expressed as S-Zn $_x$ Li) were divided into two parts. One part was further heated at 300 °C for 12 h (S-Zn $_x$ Li300).

Analysis methodology

X-ray diffraction (XRD). Powder XRD patterns were collected between 1° and 65° (2 θ) at a scanning rate of 1° min^{-1} with a step size of 0.01° (2 θ) and a fixed divergence slit size of 0. 60° (2 θ) on a Bruker D8 Advance diffractometer with Ni-filtered $CuK\alpha$ radiation ($\lambda = 0.154$ nm, 40 kV, and 40 mA). The humidity is controlled at ca. 30% by an automatic air dehumidifier. Randomly oriented samples were prepared by pressing powders inside a cavity up to the reference level of the sample holders. Oriented samples were prepared by pipetting the clay suspension onto a glass slide and allowing it to dry at room temperature. Glycolated samples were prepared by treating the oriented samples in a desiccator with ethylene glycol (EG) at 30 °C for 24 h.

Fourier transform infrared (FTIR) spectroscopy. FTIR spectra were obtained by a Bruker VERTEX 70 Fourier transform infrared spectrometer, using KBr pressed disk technique. 0.9 mg of each sample and 80 mg of KBr were well mixed and ground in an agate mortar for 15 min. The mixtures were pressed for 5 min at 10 kbar and heated under a lamp for 3 min to remove adsorbed water before FTIR measurements. All spectra were collected at room temperature over the range of 400–4000 cm^{-1} with a resolution of 4 cm^{-1} and 64 scans.

Transmission electron microscopy (TEM). TEM was performed with an FEI Talos F200S field-emission transmission electron microscope, operating at an accelerating voltage of 200 kV. Specimens were prepared by dispersing the sample in ethanol and ultrasonically treating for 5 min. A drop of the resulting dispersion was placed on a copper grid with carbon film coating, after which the ethanol was evaporated.

To investigate the stacking structures of smectites along [001], oriented samples were embedded in epoxy resin and dried at 100 °C for 3 h. Subsequently, ultrathin sections perpendicular to the film with a thickness of ~75 nm were sliced with a diamond knife using a Lecia EM UC7 ultramicrotome. The thin sections were placed on carbon-coated copper microgrids for TEM observation.

Magic-angle-spinning nuclear magnetic resonance spectroscopy (MAS NMR). ^{29}Si MAS NMR experiments were performed using a Bruker AVANCE III 600 spectrometer at resonance frequencies of 119.2 MHz. ^{29}Si MAS NMR spectra with high-power proton decoupling were recorded on a 4 mm probe with a spinning rate of 12 kHz, a $\pi/4$ pulse length of 2.6 μs , and a recycle delay of 80 s. The chemical shifts of ^{29}Si were referenced to tetramethylsilane (TMS).

Atomic pair distribution function (PDF) analysis and refinement. X-ray total scattering experiments for PDF analysis were carried out on a PANalytical Empyrean Nano with an Ag source $K\alpha_1$ ($\lambda = 0.5594214 \text{ \AA}$) and a GaliPIX 3D detector, at an operating voltage of 60 kV and an operating current of 36 mA. All data were collected at room temperature over an angular range (2θ) between 2° and 140°, with a step size of 0.0286°. Calibration of the experimental setup was done by measuring crystalline silicon (NIST Si) as a standard material to calibrate the sample-to-detector distance and to determine the Q_{damp} and Q_{broad} , which are the parameters that correct the PDF envelope function for the instrument resolution (Egami and Billinge 2012). Diffraction data of empty polyimide tube were collected with the same exposure time for background removal in the data reduction. The experimental data were converted to PDF patterns using PDFgetX3 software (Juhás et al. 2013).

Models refinement based on PDF data and crystal structure optimization. PDF structural refinement were carried out using the PDFgui software (Farrow et al. 2007). The initial models used to refine based upon PDF pattern of the Zn-sample (S-Zn4) have $C\bar{1}$ and $C2/m$ space groups modified from talc (Drits et al. 2012) and hectorite (Breu et al. 2003), respectively. Because X-ray diffraction is insensitive to H as in –OH and the main focus of our PDF local structure modeling is the intra-layer structure, H and interlayer cations were removed from the models. The structural formula for S-Zn4 model was calculated from the chemical composition determined by ICP-AES and the cation-exchange capacity. The fittings using two models for S-Zn4 were performed between $r_{\text{min}} = 1 \text{ \AA}$ and $r_{\text{max}} = 20 \text{ \AA}$. Unit-cell parameters, atomic site occupancies, atomic positions, and atomic displacement parameters (ADPs) were refined. The refined values Q_{damp} and Q_{broad} were fixed in the subsequent structural refinements of the PDF data. The atomic positions were fixed during the refinement of talc model (Drits et al. 2012), but were refined with the hectorite model under the restrictions of the space group (Breu et al. 2003).

After refinements, the unit-cell parameters, atomic coordinates, and site occupancies were input into the Materials Studio software package to further build the overall crystal structure of Zn-smectite. The H in –OH and interlayer cations were restored, which were removed previously during the models refinement using PDF data. The interlayer space was set to the d_{001} value from its XRD pattern. The H atom was added to the octahedral O that was not connected to the tetrahedron with a default O-H length (0.82 \AA) and a direction parallel to the layer stacking direction. The number (p.h.u.c.) and occupancy of interlayer cations were set according to the corrected structural formula. Their initial atomic coordinates were set to the midpoint of the two nearest –OH in the adjacent layers. Subsequently, density functional theory (DFT) based calculation was carried for the geometry optimization using Perdew-Burke-Ernzerhof (PBE) function (Perdew et al. 1996), which is simplified by generalized-gradient approximation (GGA) as in CASTEP module (Clark et al. 2005). A $3 \times 2 \times 1$ k-points sampling grid was set for the optimization. The cutoff energy of the projector augmented plane-wave basis was set at 598.7 eV to ensure energy accuracy. The full geometry optimizations were carried out with convergence thresholds of 1.0×10^{-5} eV and 0.03 eV/ \AA for total energy and maximum force, respectively.

RESULTS

XRD results of hydrothermal products

XRD patterns of the synthetic samples showed a series of reflections at 2θ angles ca. 5.84, 19.58, 28.78, 35.31, 59.70°, etc., close to those of saponite (a Mg-rich trioctahedral smectite) and other smectites (Fig. 1) (Faust et al. 1959; Petit et al. 2008; Tao et al. 2016). The d value of the 001 reflection was ca. 12.8 \AA for the S-Zn4 sample, which is typical for smectite (Bergaya and Lagaly 2013). All the other patterns in the range of 15 to 40° (2θ) exhibit broad and asymmetric reflection maxima, typical of turbostratically stacked smectites. The d values of the diagnostic reflection 06 l band at ca. 60° (2θ) are all larger than 1.525 \AA , indicating that the samples are trioctahedral (Bergaya and Lagaly 2013).

With the increase in the Zn/Mg ratio, the relative intensity of the 001 reflection was prominently increased, while the full-width at half maximum (FWHM) decreased from 6.44° (2θ) for S-Zn1 to 1.33° (2θ) for S-Zn4. The sample in which octahedral sites were only occupied by Zn (Fig. 1d) shows the narrowest and sharpest 001 reflection with the highest intensity. After EG saturation, all samples except S-Zn1_EG (Fig. 2) showed increase in the relative intensity of the 001 reflections (16.2 \AA).

^{29}Si MAS NMR Spectra of hydrothermal products

The nearest neighbor environment of Si was assessed by ^{29}Si MAS NMR spectra. Q^m ($m = 0, 1, 2, 3, \text{ and } 4$) was adopted to describe the Si environments in the solid products, in which Q^m refers to the polymerization state of Si (Tao et al. 2016). Two main signals were recorded at ca. –95.0 and –83.8 ppm (Fig. 3) for all the as-synthesized samples, which are attributed to Q^3 Si

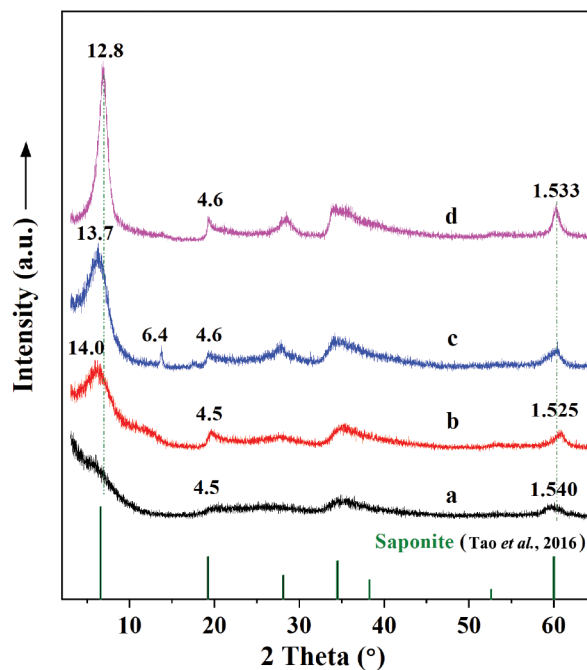


FIGURE 1. XRD patterns of the samples with different concentrations of Zn and Mg in octahedral sheet. (a) S-Zn1, (b) S-Zn2, (c) S-Zn3, and (d) S-Zn4. (Color online.)

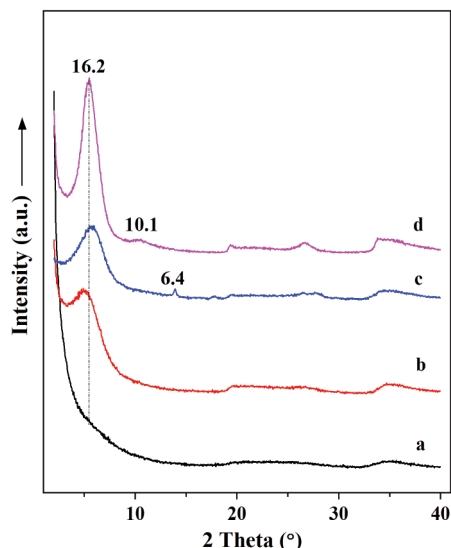


FIGURE 2. XRD patterns of EG saturated samples: (a) S-Zn1EG, (b) S-Zn2EG, (c) S-Zn3EG, and (d) S-Zn4EG. (Color online.)

and Q² Si, respectively. Signals at ca. 110 ppm are ascribed to amorphous silica, as in all the samples except for S-Zn4.

TEM images of hydrothermal products

Typical flaky grains with curled ribbon-like edges were observed in TEM images for all products (Fig. 4). This is a very common morphology for smectite minerals, such as saponite and saunonite (Güven 1988; Schingaro et al. 2021; Tao et al. 2019). Among the products, S-Zn1 displayed the smallest particle sizes (Fig. 4a). There were loose, fluffy, needle-like fine grains randomly aggregated on its surface with a thickness of several nanometers along the direction perpendicular to the crystal plates (*c** direction). This is probably the lateral view of the particles, and they were possibly formed by the curling of the very thin smectite layers. Similar aggregations were also observed in S-Zn3 (Fig. 4c). The S-Zn4 sample was readily identified because it had the largest particle size (Fig. 4d).

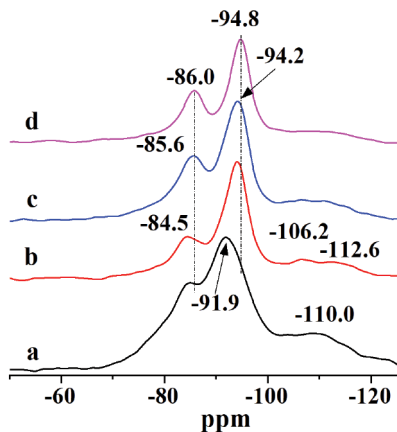


FIGURE 3. ²⁹Si MAS NMR spectra of synthesized samples: (a) S-Zn1, (b) S-Zn2, (c) S-Zn3, and (d) S-Zn4. (Color online.)

Turbostratic layer stacking could be further evidenced by selected area electron diffraction (SAED) of the samples. However, for such hydrated clay minerals, all attempts to obtain their SAED failed due to the structural damage caused by the electron beam under the vacuum of the TEM. Fortunately, lateral lattice images mostly along *a* or *b* directions of the S-Zn4 grain were successfully obtained from ultrathin sections of oriented samples embedded by epoxy (Fig. 5). In the HRTEM image, the lateral stacking of layers along the *c* direction could be clearly seen. The orientation could be verified by the single layer distance (orange bar), which was calculated to be ca. 130–140 Å, close to 10 times of the *d*₀₀₁ value of S-Zn4 (Fig. 1). The fast Fourier transform (FFT) of the HRTEM image was processed for the selected areas 1 and 2 (Fig. 5). Although the diffraction spots were not clear, they still could be recognized, which showed a ~12.5 Å *d*-spacing (Figs. 5 and 2). This value is also in accord with the *d* value determined by XRD (Fig. 1). The turbostratic nature of the crystal layer could be visually observed by the randomly distributed single layers (orange arrow).

DISCUSSION

Chemical compositions and origin of permanent layer charge

Considering that ²⁹Si MAS NMR spectrum of S-Zn4 shows the least and negligible amount of amorphous silica (Fig. 3), its chemical composition and the formula calculated from it are much closer to the pure phase than those of all other products. Therefore, elemental analyses of S-Zn4 and its Li⁺ exchanged product were performed by ICP-AES (Table 1), in which each value is the average of three parallel tests. The synthesis of a pure sample with only Mg²⁺ in octahedral sites (stevensite) turned out to be a XRD amorphous magnesium gel (not shown), which may require much higher temperature and pressure to crystallize than those used in this study (Golubeva et al. 2005). The composition of S-Zn4 mainly consisted of silicon, zinc, sodium and magnesium. Si always occupies tetrahedral sites in a smectite structure, Zn and Mg generally occupy octahedral sites, and Na appear preferentially in the interlayers. The calculation from chemical analyses showed that the total contents of Zn was insufficient for the occupancy of all the octahedral sites (Schlesinger et al. 2021). Some vacancies therefore must exist in the octahedral sheet to keep the ratio of T/O at 4:3 and generate permanent layer charge. This kind of structure has commonly been found for ferric, nickel, or magnesium trioctahedral smectites, which generates the layer charge together with the effect of substitution in tetrahedral or/and octahedral sheets from ca. 0.15e⁻ to 0.56e⁻ p.h.u.c. (Christidis and Mitsis 2006; Hicks et al. 2014; Takahashi et al. 1997; Vicente et al. 1996).

Layer charge is an important characteristic of 2:1 smectites. It is not only a criterion for the classification of smectites but also influences the capacity to retain cations and to adsorb H₂O and polar organic molecules (Boyd et al. 1994). The layer charge of smectites arises primarily from the permanent charges generated by isomorphous substitutions in their structures. Generally, both tetrahedral and octahedral sheets can have these substitutions. For instance, in tetrahedral sheets, there are often trivalent cation (typically Al³⁺, Fe³⁺) substitutions for Si⁴⁺, whereas in octahedral

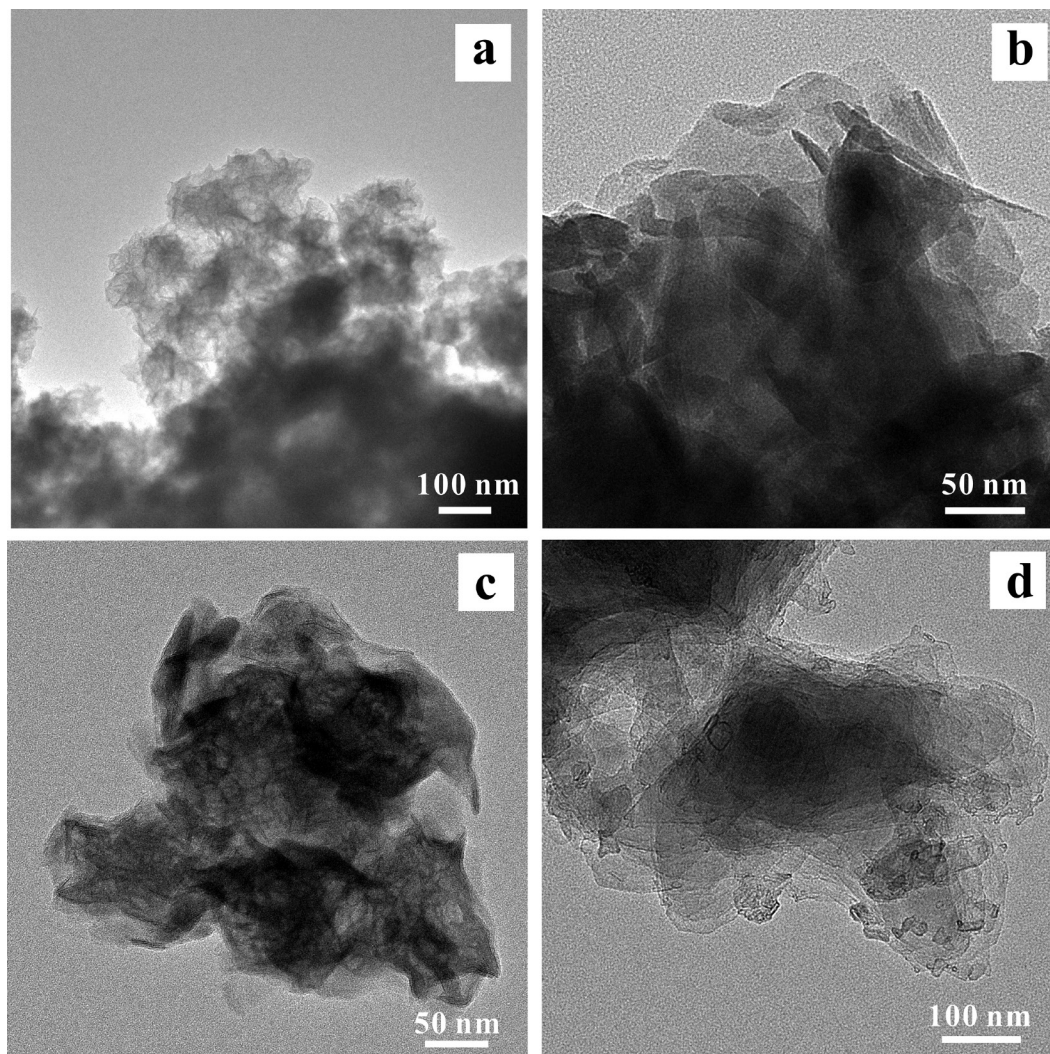


FIGURE 4. TEM images of synthesized samples: (a) S-Zn1, (b) S-Zn2, (c) S-Zn3, and (d) S-Zn4.

sheets, substitutions involve Mg^{2+} , Al^{3+} , Fe^{3+} , Li^{+} , etc. (Bergaya and Lagaly 2013). Two types of octahedral substitutions generally occur. One involves the substitution of 3 bivalent cations by 2 trivalent cations and a vacancy ($3Mg^{2+} = 2Al^{3+} + \square$) (Kloprogge et al. 1994). The other is a one-to-one model, in which 1 Al^{3+} is replaced by 1 Mg^{2+} (Suquet et al. 1981). The former substitution has no effect on the layer charge, whereas the latter generates a positive charge. In addition, there are also some special smectites (e.g., stevensite), whose layer charge is generated by the presence of cation deficiencies (vacancies) either in octahedral or tetrahedral sheets, or both, or even with no cation substitution (Bergaya and Lagaly 2013; Suquet et al. 1981).

NMR spectra (Fig. 3) showed that with increasing Zn/Mg, both Q^3 Si and Q^2 Si are intensified and increased in symmetry along with a decrease in peak width and an increase in chemical shift (negative). Meanwhile, the intensity of the broad signals at ca. -100 ppm decreased, corresponding to the gradual reduction of the amorphous silica phase. If all three octahedral sites are occupied by Mg^{2+} , four Si^{4+} tetrahedra are required p.h.u.c.

to form the ideal 2:1 type of trioctahedral smectite structure ($Si/Mg = 4:3$). Considering that the concentration of Si was sufficient in the raw materials, excess Si allowed the amorphous silica phase to precipitate in the products. The least and negligible amount of amorphous silica for S-Zn4 as shown by ^{29}Si MAS NMR spectrum (Fig. 3a), indicates that most of the input Si participated in the formation of Zn-smectite. It requires more Zn than the input to maintain the ideal T:O ratio of 4:3 for a trioctahedral structure, which therefore leads to the possibility that some cationic defects exist in the octahedral sheets of the zinciferous products, similar to those in ZnO semiconductors (Fabbri et al. 2014; Janotti and Van de Walle 2009; Pan et al. 2014). Actually, many elements, such as Mg, Fe and Ni, can form this kind of octahedral vacancy with generated layer charge, similar to that in stevensite and zincsilite, which can be deduced from the perspective of layer charge balance. The lowest amount of amorphous silica in S-Zn4 product compared with the other products also implies that Zn is much easier than Mg to react with Si and crystallize to form smectite with octahedral defects.

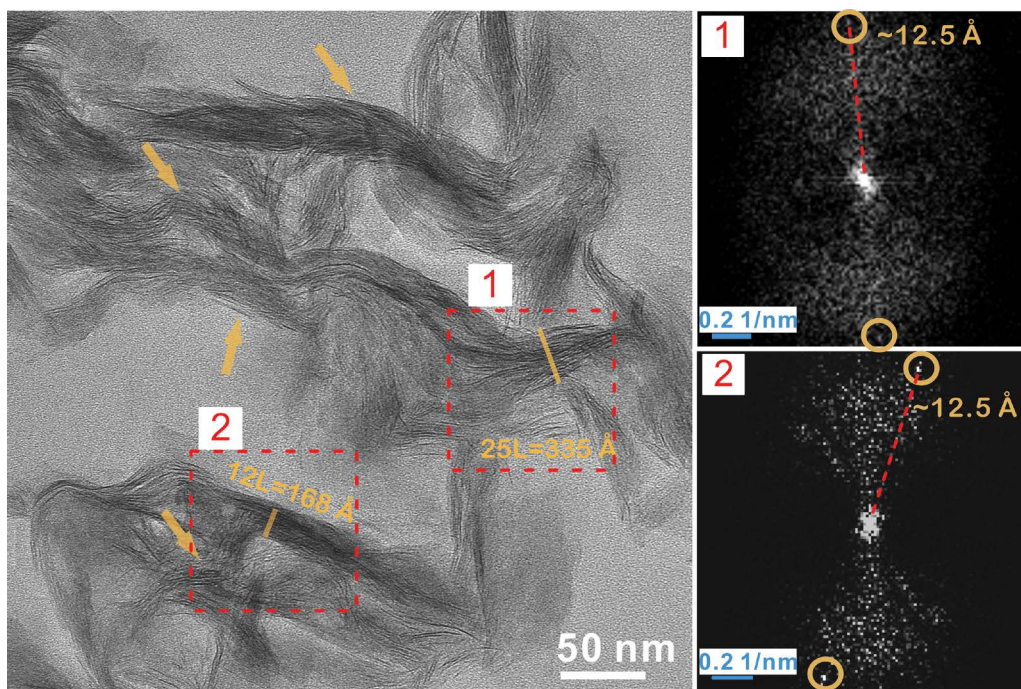


FIGURE 5. HRTEM image of the ultrathin section of S-Zn4 with the turbostratically disordered layers. L represents the thickness of a layer. The arrows indicate the areas where the layers are stacked in random orientations. (Color online.)

The layer charge of smectite was mainly contributed by permanent charge (Petit et al. 1995). The CECs of all samples have been determined to estimate their layer charges here (Table 2). All samples showed larger CECs (over 109 mmol/100 g) than those of typical dioctahedral smectites (e.g., montmorillonite) and were comparable to those of synthesized trioctahedral smectites (e.g., saponite) determined by the same processes (He et al. 2014). The proportion of tetrahedra (T) is 4 in p.h.u.c. for an ideal smectite. In this study, the input Si is excessive, and there are no other cations that can enter tetrahedra sites. Based on the CEC value of S-Zn4 and fixing the ratio of Si as 4 in p.h.u.c., the theoretical proportions of interlayer cations (represented as Mi^+ , e.g.,

Na^+), octahedral Zn, and vacancies are calculated as 0.58, 2.71, and 0.29, respectively. Therefore, the ideal structural formula of S-Zn4 can be presented as $Zn_{0.27}Na_{0.04}(Zn_{2.71}\square_{0.29})Si_4O_{10}(OH)_{12}$ (Table 2). According to the statistics in the literature, there are usually at least 2.75 octahedral sites that should be occupied for the trioctahedral smectites, whose charges were generated by isomorphic substitutions (Hutton 1947). The number of occupied octahedral sites is smaller than the value in this case, suggesting the occurrence of octahedral Zn defects. The calculated layer charge p.h.u.c. (0.58) indicates that the obtained product belongs to high-charge trioctahedral smectites (0.48–0.60 e p.h.u.c.) (Christidis and Mitsis 2006; Milesi et al. 2019).

TABLE 1. The chemical compositions (wt%) by ICP-AES of the products

Samples	SiO ₂	ZnO	Na ₂ O	Li ₂ O	Else ^a	L.O.I.	Total (%)
S-Zn4	49.70	41.30	0.67	–	0.14	7.13	98.94
S-Zn4-Li	49.40	40.90	0.05	0.23	0.17	8.09	98.84

^a“Else” includes those not intended to input as source chemicals and with trace amounts of contents, such as Ca, Fe, Al, and Ti.

TABLE 2. CECs and calculated structural formulas of as-synthesized samples

Samples	CECs (mmol/100 g)	Structural formulas	
		Calculated by CECs ^a	Corrected by compositions
S-Zn1	115.7	^b $Mi_{0.58}[(Zn,Mg)_{2.71}\square_{0.29}]Si_4O_{10}(OH)_2$	N.D.
S-Zn2	109.5	$Mi_{0.54}[(Zn,Mg)_{2.73}\square_{0.27}]Si_4O_{10}(OH)_2$	N.D.
S-Zn3	114.4	$Mi_{0.57}[(Zn,Mg)_{2.72}\square_{0.28}]Si_4O_{10}(OH)_2$	N.D.
S-Zn4	117.4	$Mi_{0.58}(Zn_{2.71}\square_{0.29})Si_4O_{10}(OH)_2$	$Zn_{0.27}Na_{0.04}(Zn_{2.71}\square_{0.29})Si_4O_{10}(OH)_2$

Notes: N.D. = Not determined.

^a Calculation method: The proportion of Si (excessive) p.h.u.c. was set to 4.

^b Mi represents the interlayer cation.

It was also noticed that most of the interlayer cations are Zn^{2+} for S-Zn4 (Table 2). It was probably because there were no other cations available, with the exception of Na^+ , during the formation of S-Zn4. This is obviously different from the structure of saunonite, in which Zn is mainly located within the octahedral site, and the Zn^{2+} adsorbed at the mineral surface or fixed in the interlayer is negligible or lacking (Schingaro et al. 2021).

Layer charge position and its effects on the expandability of Zn-smectite: Hoffmann-Klemen effects

Previous research revealed that dioctahedral clay minerals saturated with small cations such as Li^+ (ionic radius 0.90 Å) lose their cationic exchangeability after being heated at ca. 250 °C for 24 h (Hofmann and Klemen 1950). As there are ~1/3 unoccupied octahedral sites, the migration of Li^+ cations toward the vacant octahedral sites appreciably reduces the octahedral layer charge. Migration of Li to the ditrigonal cavities when heated is also a common phenomenon for dioctahedral smectites

(e.g., beidellite), whose layer charges can be generated only by tetrahedral substitutions (Komadel et al. 2005). In contrast, this effect does not occur in trioctahedral smectites (e.g., hectorite) (Glaeser and Mering 1971).

In this case, there are ca. a total of 1/10 vacant octahedral sites for S-Zn4 (Table 2), and interlayer Li^+ can migrate to these sites during the heating treatment. Although the CEC value of the Li-saturated sample is reduced to 27.13 mmol per 100 g, the heated Li-bearing sample still shows an increased d_{001} value as 16.2 Å in the XRD pattern (Fig. 6). This indicates that the adjacent TOT layers were not “locked”/collapsed, demonstrating that the layer charge was generated by the vacancies in the octahedral sites instead of isomorphous substitutions in tetrahedral sheets.

After Li fixation, the Si-O-Si stretching bands become obviously narrower and shifted to higher frequencies (up to 1019 cm^{-1}) than those of unheated samples (Fig. 7). This trend is consistent with that for the reduced-charge montmorillonite (Madejová et al. 1996), reflecting the variation of magnitude and location of layer charge (Kitajima et al. 1991). Based on the results above, the products synthesized here were determined to be zincsilite-like smectites.

Characterization of the local structure of zincsilite by PDF analysis

To obtain the crystal structure of S-Zn4, PDF analysis was applied because it is very sensitive to short- and medium-range order. The decay of the PDF pattern for S-Zn4 from low- to high- r regions suggested a ~ 24 Å coherent crystalline domain size (intra-layer domain). The value is consistent with the height of ca. 2 TOT layers (Fig. 1).

The PDF peaks represent interatomic distances in the structure. The first peak at ~ 1.58 Å corresponds to Si-O correlations in the tetrahedral sheet (Figs. 8 and 9a'). The second peak at ~ 2.16 Å is consistent with Zn-O correlations in the octahedral sheet (Figs. 8 and 9a'). The third peak at ~ 3.11 Å may consist of three kinds of correlations, including the neighboring tetrahedral Si atoms

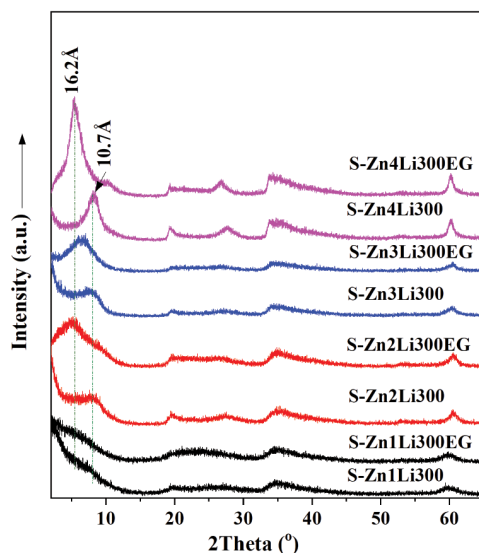


FIGURE 6. XRD patterns of the EG-saturated samples after H-K effect tests. (Color online.)

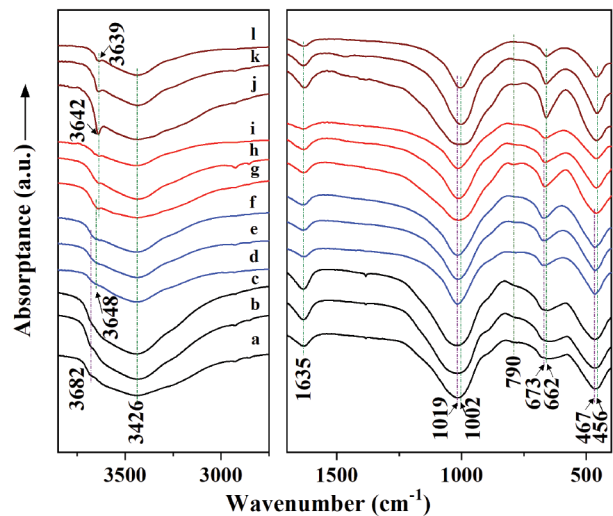


FIGURE 7. FTIR spectra of Co exchanged samples (after CECs tests), Li exchanged samples, and 300 °C heated Li exchanged samples. (a) S-Zn1Co, (b) S-Zn1Li, (c) S-Zn1Li300, (d) S-Zn2Co, (e) S-Zn2Li, (f) S-Zn2Li300, (g) S-Zn3Co, (h) S-Zn3-Li, (i) S-Zn3Li300, (j) S-Zn4Co, (k) S-Zn4-Li, and (l) S-Zn4Li300. (Color online.)

that share a basal O, the neighboring octahedral Zn atoms, and the adjacent apical O atoms that bridge tetrahedral Si and octahedral Zn (Figs. 8 and 9a'). The peak at ~ 5.39 Å is consistent with Si-Si correlations at the diagonal position in the interconnected six-membered SiO_4 rings, which may overlap with the correlations of the second nearest Zn-Zn (Figs. 8 and 9a').

The selected models, i.e., talc and hectorite, have different symmetries. Talc has a lower symmetry ($C\bar{1}$) than hectorite ($C2/m$). The refined results using the talc model are almost in perfect agreement with the experimental PDF data in the region of 1.0 to 20 Å (Figs. 9a and a'). The difference between the experimental and calculated patterns is as low as 0.037 (R_w) for ca. 10% vacancies random distributed in octahedral sheet (Table 2; Fig. 9a). Although the calculated PDF pattern of modi-

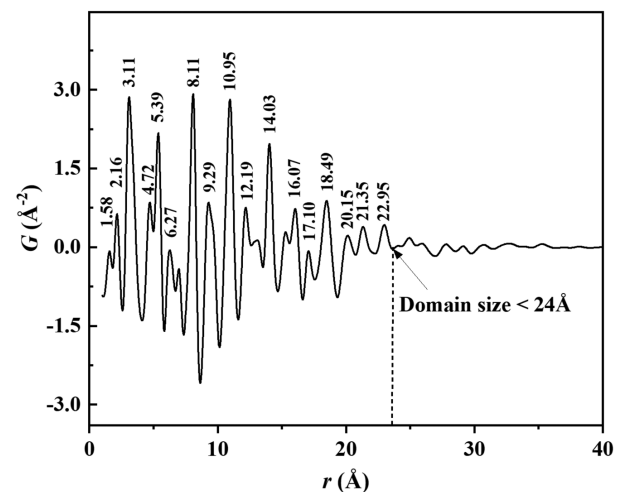


FIGURE 8. The experimental PDF data of S-Zn4 from 1 to 40 Å range. The decay of the pattern suggests a ~ 24 Å coherent crystalline domain.

fied hectorite (interlayer cations removed) matches reasonably ($R_w = 0.206$) with the peak positions of the experimental data (Fig. 9b), obvious distortions could be clearly observed by the mismatches in almost all peaks more or less (Figs. 9b and 9b'). A further check of the refined structure indicated that distorted bonds were generated during the refinement processes, such as Si-O (Figs. 9b and 9b'). These distortions could also result from the Zn vacant sites, similar to those observed for layered vernadite (Lee and Xu 2020). They could further reduce the symmetry of phase, which is probably the reason why the talc model shows better match with the experimental PDF pattern than that of the hectorite framework.

To build the structure of zincsilite, the refined unit-cell parameters, atomic coordinates, and site occupancies using the talc model were imported into Material Studio software. The interlayer space was set to 12.800 Å according to XRD pattern

(Fig. 1). The H in hydroxyl groups was added to parallel with the layer stacking direction (c^* directions). The amount of interlayer cations (1 for 4 Si in p.h.u.c) and their occupancies (0.58) were set according to the corrected structural formula. The initial atomic coordinates of the interlayer cations were set to the midpoint of the two adjacent hydroxyl groups in the c^* direction. After optimization, the space group of the crystal changes to $P\bar{1}$ and the cell parameters are as follows: $a = 5.294$ Å, $b = 9.162$ Å, $c = 12.800$ Å, $\alpha = 90.788^\circ$, $\beta = 98.345^\circ$, and $\gamma = 90.399^\circ$ (Fig. 10 and CIF¹).

CONCLUDING REMARKS

Obtaining the reliable crystal structure of smectite by only analyzing its XRD reflections is very challenging because of its small crystallite size and the occurrence of extensive stacking disorder among the layers. In this study, zincsilite-like smectite

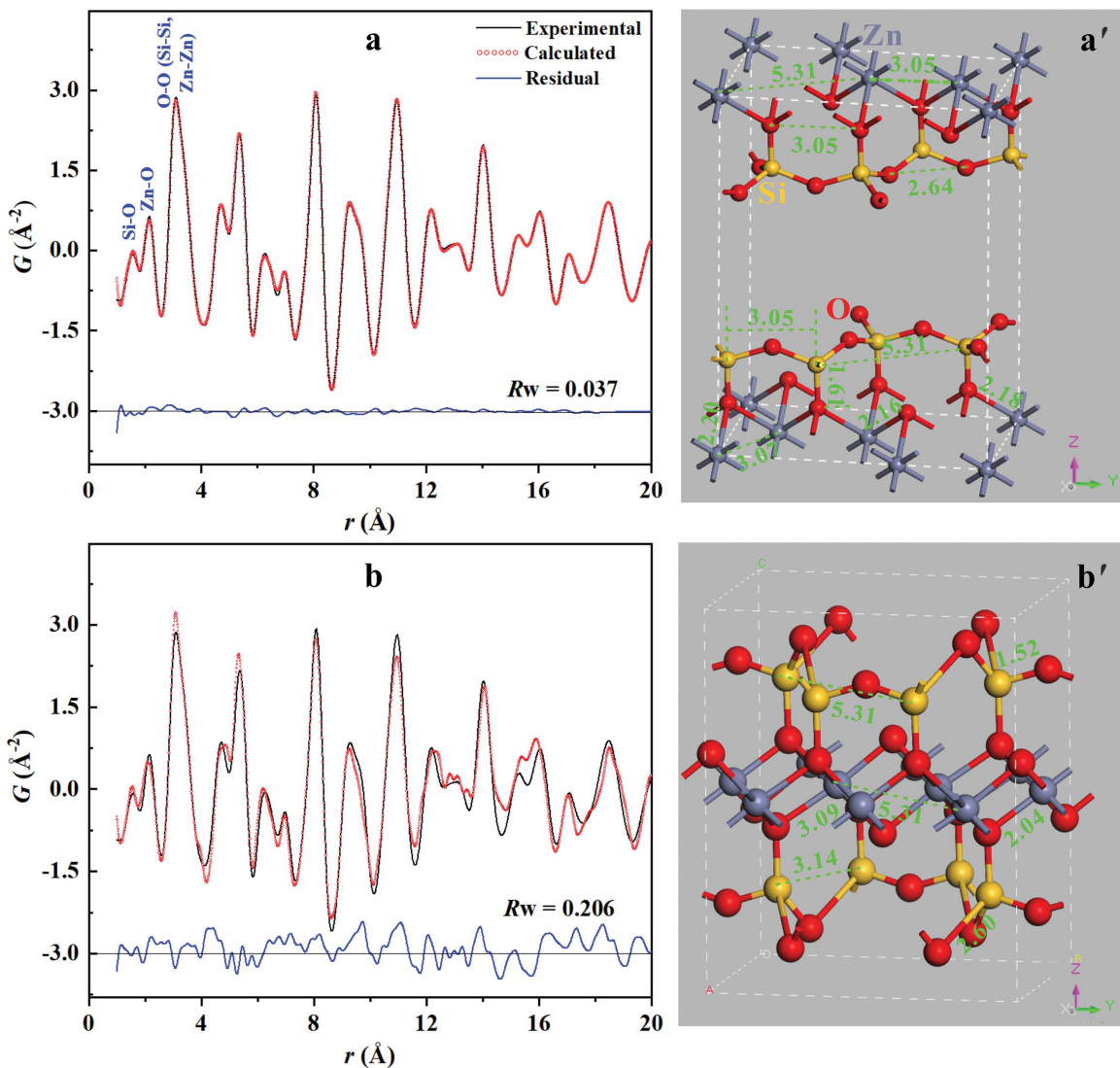


FIGURE 9. PDF patterns of S-Zn₄ from 1 to 20 Å range and related refinements using different models: (a) Talc with a triclinic symmetry and a $C1$ space group. (b) Hectorite with a monoclinic symmetry and a $C2/m$ space group. a' and b' show the interatomic distances in the resulted structures. (Color online.)

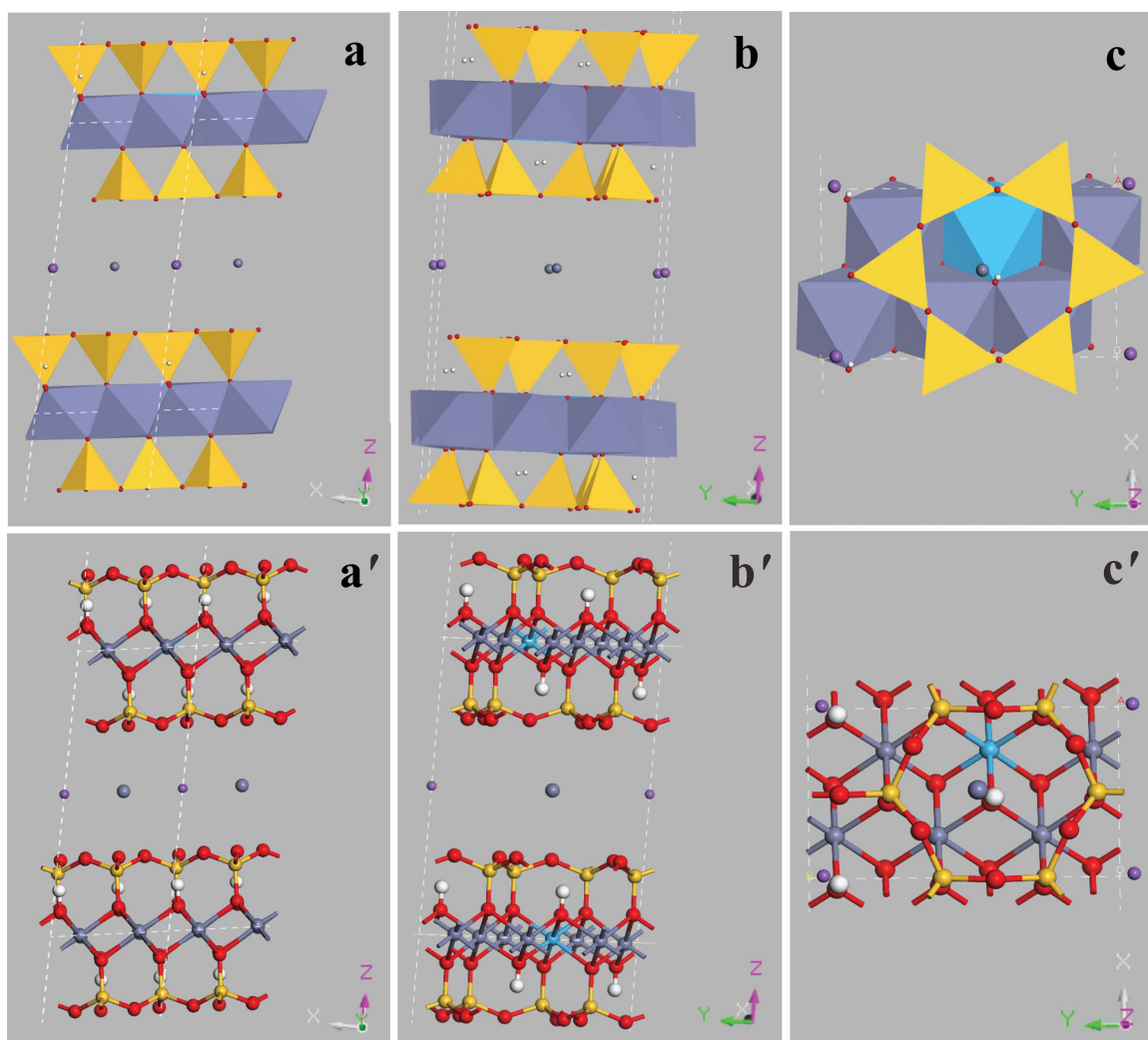


FIGURE 10. The front (a and a'), side (b and b'), and top (c and c') views of optimized crystal structure of zincsilitite. The octahedra and atoms in blue represent octahedral Zn defects. (Color online.)

has been successfully synthesized, whose layer charge was generated by the Zn defects in octahedral sheets. XRD and TEM results showed that turbostratically disordered layer stacking existed in their grains. PDF analysis indicated that zincsilitite only has a short-range order with a domain size of ca. 24 Å (2 layers). Further refinement reveals that the structure of the synthetic zincsilitite fits talc with a triclinic symmetry better than hectorite with a monoclinic symmetry. The lower symmetry of this zincsilitite compared with common smectites could be attributed to its bond distortions in both tetrahedral and octahedral sheets, which probably result from the octahedral Zn defects. Finally, the crystal structure of zincsilitite was built and optimized using DFT calculation in CASTEP module of Materials Studio software with the unit-cell parameters obtained by the talc model refinement based upon PDF data, restoring interlayer cations and H atoms in hydroxyl groups, and setting c value according to XRD results. The optimized structure has a $P\bar{1}$ space group, and the unit-cell parameters obtained are $a = 5.294$ Å, $b = 9.162$ Å, $c = 12.800$ Å,

$\alpha = 90.788^\circ$, $\beta = 98.345^\circ$, and $\gamma = 90.399^\circ$.

Due to the variable compositions, fine crystallite sizes, difficulty to synthesize single crystals, and the widespread turbostratically disordered layers (Ufer et al. 2004), XRD patterns of smectites contain no 3D information, and therefore, it is inapplicable to determine their crystal structures by traditional refinement method. Meanwhile, as they are hydrated minerals with very fragile layers, it is also very challenging to obtain complete and reliable SAED patterns for crystal structure analysis. Although smectite models can be constructed by XRD refinement, special techniques must be adopted to increase the layer stacking order, such as using F to replace -OH for hectorite structure determination (Breu et al. 2003); otherwise, the obtained model actually represents merely the short-range ordered domains. How to directly, quickly, and accurately obtain the crystal structure parameters and models of smectites has been a continuous problem for decades.

This study reports a novel method to determine the crystal structure of smectite by using a combination of the model

refinement based on PDF data and structure optimization by DFT calculation. Among them, PDF analysis provides accurate distance information between atoms using the real-space refinement method (Billinge and Kanatzidis 2004; Lee and Xu 2020), which does not depend on the long-distance order of the structure (Egami and Billinge 2012). Meanwhile, DFT calculation can optimize the positions of H atoms in –OH and interlayer cations. Although zinsilite has more octahedral defects than other common trioctahedral smectites, the method is believed still effective for all smectites with both di- and tri-octahedral structures, as well as the other materials and minerals with turbostratically disordered layers, such as graphite and illite-smectites interstratified clay minerals (Neder and Proffen 2008).

The CEC value shows that the amount of the charge reaches 117 mmol per 100 g for zinsilite, which is comparable to those of common trioctahedral smectites (He et al. 2014). Because there is no substitution in either tetrahedral or octahedral sheets of zinsilite, and its structure did not irreversibly collapse after heating the Li⁺-saturated sample to 300 °C (Hoffmann-Klemen effects), the layer charge of zinsilite is deduced as generated by the Zn vacancies (defects) in the octahedral sites. Generally, Hoffmann-Klemen effect is much more common for dioctahedral smectites (such as beidellite) (Komadel et al. 2005), while it does not occur in trioctahedral smectites (such as hectorite) (Glaeser and Mering 1971). It is therefore inferred that the expandability of zinsilite with layer charge generated by octahedral vacancies is different from that of common trioctahedral smectites, whose charges are generated by isomorphous substitution and are similar to those of dioctahedral smectites.

In short, smectites are made of turbostratically disordered layers along their stacking directions, which makes it impossible to build their 3D crystal structures. However, their local domain structures (such as intralayer structure) can be reliably determined by PDF methods.

ACKNOWLEDGMENTS

The authors are grateful to Simon Billinge at Columbia University for the suggestions on PDFgui parameter setting and crystal structure modeling. We thank Kristian Ufer and Reinhard Kleeberg at TU Bergakademie Freiberg, and Gennaro Venturi at University of Bari for kindly providing smectites models and helping with XRD profile refinement using BGMN. We also appreciate Junliang Sun and Yaming Qiu at Peking University for constructive suggestions on crystal structure determination and XRD profile refinement.

FUNDING

This work was financially supported by the National Natural Science Foundation of China (Grant Nos. 41921003, 42072044, and 42272038), Basic Public Welfare Research Project of Zhejiang Province (LGC21D010001), and Science and Technology Planning of Guangdong Province, China (2020B1212060055).

REFERENCES CITED

- Anthony, J.W., Bideaux, R.A., Bladh, K.W., and Nichols, M.C., Eds. (2001) *Handbook of Mineralogy*. Mineralogical Society of America, Chantilly.
- Artioli, G., Bellotto, M., Gualtieri, A., and Pavese, A. (1995) Nature of structural disorder in natural kaolinites, a new model based on computer simulation of powder diffraction data and electrostatic energy calculation. *Clays and Clay Minerals*, 43, 438–445, <https://doi.org/10.1346/CCMN.1995.0430407>.
- Bergaya, F. and Lagaly, G. (2013) *Handbook of Clay Science*, 2nd ed., 1224 p. Elsevier.
- Billinge, S.J.L. and Kanatzidis, M.G. (2004) Beyond crystallography: The study of disorder, nanocrystallinity and crystallographically challenged materials with pair distribution functions. *Chemical Communications*, 35, 749–760, <https://doi.org/10.1039/b309577k>.
- Bisio, C., Gatti, G., Boccaleri, E., Marchese, L., Superti, G.B., Pastore, H.O., and Thommes, M. (2008) Understanding physico-chemical properties of saponite synthetic clays. *Microporous and Mesoporous Materials*, 107, 90–101, <https://doi.org/10.1016/j.micromeso.2007.05.038>.
- Boyd, S.A., Farmer, W.J., Jaynes, W.F., Lagaly, G., Laird, D.A., and Mermut, A.R. (1994) Layer charge characteristics of 2:1 silicate clay minerals. In A.R. Mermut, Ed., *Clay Minerals Society, Workshop Lectures*, vol. 6, 10 p. <https://doi.org/10.1346/CMS-WLS-6>.
- Braunbarth, C., Hillhouse, H.W., Nair, S., Tsapatsis, M., Burton, A., Lobo, R.F., Jacubinas, R.M., and Kuznicki, S.M. (2000) Structure of strontium ion-exchanged ETS-4 microporous molecular sieves. *Chemistry of Materials*, 12, 1857–1865, <https://doi.org/10.1021/cm9907211>.
- Breu, J., Seidl, W., and Stoll, A. (2003) Fehlordnung bei smectiten in abhängigkeit vom zwischenschichtkation. *Zeitschrift für Anorganische und Allgemeine Chemie*, 629, 503–515, <https://doi.org/10.1002/zaac.200390083>.
- Brindley, G.W. and Brown, G. (1980) *Crystal Structures of Clay Minerals and Their X-ray Identification*, 518 p. Mineralogical Society of Great Britain and Ireland.
- Casas-Cabanas, M., Reynaud, M., Rikarte, J., Horbach, P., and Rodríguez-Carvajal, J. (2016) FAULTS: A program for refinement of structures with extended defects. *Journal of Applied Crystallography*, 49, 2259–2269, <https://doi.org/10.1107/S1600576716014473>.
- Christidis, G.E. and Mitsis, I. (2006) A new Ni-rich stevensite from the ophiolite complex of Othrys, central Greece. *Clays and Clay Minerals*, 54, 653–666, <https://doi.org/10.1346/CCMN.2006.0540601>.
- Clark, S.J., Segall, M.D., Pickard, C.J., Hasnip, P.J., Probert, M.I.J., Refson, K., and Payne, M.C. (2005) First principles methods using CASTEP. *Zeitschrift für Kristallographie–Crystalline Materials*, 220, 567–570, <https://doi.org/10.1524/zkri.220.5.567.65075>.
- Debye, P. (1915) Zerstreuung von röntgenstrahlen. *Annalen der Physik*, 351, 809–823, <https://doi.org/10.1002/andp.19153510606>.
- Drits, V.A., Guggenheim, S., Zviagina, B.B., and Kogure, T. (2012) Structures of the 2:1 layers of pyrophyllite and talc. *Clays and Clay Minerals*, 60, 574–587, <https://doi.org/10.1346/CCMN.2012.0600603>.
- Egami, T. and Billinge, S.J.L. (2012) *Underneath the Bragg Peaks: Structural Analysis of Complex Materials*. Volume 16, Elsevier.
- Fabbri, F., Villani, M., Catellani, A., Calzolari, A., Cicero, G., Calestani, D., Calestani, G., Zappettini, A., Dierre, B., Sekiguchi, T., and others. (2014) Zn vacancy induced green luminescence on non-polar surfaces in ZnO nanostructures. *Scientific Reports*, 4, 5158, <https://doi.org/10.1038/srep05158>.
- Farrow, C.L., Juhás, P., Liu, J.W., Bryndin, D., Božin, E.S., Bloch, J., Proffen, T., and Billinge, S.J. (2007) PDFfit2 and PDFgui: Computer programs for studying nanostructure in crystals. *Journal of Physics Condensed Matter*, 19, 335219, <https://doi.org/10.1088/0953-8984/19/33/335219>.
- Faust, G.T., Hathaway, J.C., and Millot, G. (1959) A restudy of stevensite and allied minerals. *American Mineralogist*, 44, 342–370.
- Glaeser, R. and Mering, J. (1971) Migration of Li cations in dioctahedral smectites (Hofmann-Klemen effect). *Comptes Rendus Hebdomadaires des Séances de l'Académie des Sciences. D. Science and Nature*, 273, 2399–2402.
- Golubeva, O.Yu., Korytkova, E.N., and Gusarov, V.V. (2005) Hydrothermal synthesis of magnesium silicate montmorillonite for polymer-clay nanocomposites. *Russian Journal of Applied Chemistry*, 78, 26–32, <https://doi.org/10.1007/s11167-005-0225-z>.
- Gualtieri, A.F. (1999) Modelling the nature of disorder in talc by simulation of X-ray powder patterns. *European Journal of Mineralogy*, 11, 521–532, <https://doi.org/10.1127/ejm/11/3/0521>.
- Gualtieri, A.F., Ferrari, S., Leoni, M., Grathoff, G., Hugo, R., Shatnawi, M., Paglia, G., and Billinge, S. (2008) Structural characterization of the clay mineral illite-1M. *Journal of Applied Crystallography*, 41, 402–415, <https://doi.org/10.1107/S0021889808004202>.
- Güven, N. (1988) Smectites. *Reviews in Mineralogy and Geochemistry*, 19, 497–559.
- He, H., Li, T., Tao, Q., Chen, T., Zhang, D., Zhu, J., Yuan, P., and Zhu, R. (2014) Aluminum ion occupancy in the structure of synthetic saponites: Effect on crystallinity. *American Mineralogist*, 99, 109–116, <https://doi.org/10.2138/am.2014.4543>.
- Hicks, L.J., Bridges, J.C., and Gurman, S.J. (2014) Ferric saponite and serpentine in the nakhlite martian meteorites. *Geochimica et Cosmochimica Acta*, 136, 194–210, <https://doi.org/10.1016/j.gca.2014.04.010>.
- Hillier, S. (2003) Clay mineralogy. In G.V. Middleton, M.J. Church, M. Coniglio, L.A. Hardie, and F.J. Longstaffe, Eds., *Encyclopedia of Sediments and Sedimentary Rocks*, p. 139–142. Springer.
- Hines, D.R., Seidler, G.T., Treacy, M.M.J., and Solin, S.A. (1997) Random stacking of a commensurate guest layer in an ordered host: NiAl layer-double-hydroxides. *Solid State Communications*, 101, 835–839, [https://doi.org/10.1016/S0038-1098\(96\)00682-5](https://doi.org/10.1016/S0038-1098(96)00682-5).
- Hofmann, U. and Klemen, R. (1950) Verlust der austauschfähigkeit von lithiumionen an bentonit durch erhitzen. *Zeitschrift für Anorganische Chemie*, 262, 95–99, <https://doi.org/10.1002/zaac.19502620114>.
- Hutton, C.O. (1947) Contribution to the mineralogy of the New Zealand, part 3. *Transactions of the Royal Society of New Zealand*, 76, 481–491.
- Janotti, A. and Van de Walle, C.G. (2009) Fundamentals of zinc oxide as a semiconductor. *Reports on Progress in Physics*, 72, 126501, <https://doi.org/10.1088/0034-4885/72/12/126501>.
- Juhás, P., Granlund, L., Gujarathi, S.R., Duxbury, P.M., and Billinge, S.J.L. (2010)

- Crystal structure solution from experimentally determined atomic pair distribution functions. *Journal of Applied Crystallography*, 43, 623–629, <https://doi.org/10.1107/S002188981000988X>.
- Juhás, P., Davis, T., Farrow, C.L., and Billinge, S.J.L. (2013) PDFgetX3: A rapid and highly automatable program for processing powder diffraction data into total scattering pair distribution functions. *Journal of Applied Crystallography*, 46, 560–566, <https://doi.org/10.1107/S0021889813005190>.
- Kitajima, K., Taruta, S., and Takusagawa, N. (1991) Effects of layer charge on the IR spectra of synthetic fluorine micas. *Clay Minerals*, 26, 435–440, <https://doi.org/10.1180/claymin.1991.026.3.13>.
- Kloprogge, J.T., Breukelaar, J., Geus, J.W., and Jansen, J.B.H. (1994) Characterization of Mg-saponites synthesized from gels containing amounts of Na⁺, K⁺, Rb⁺, Ca²⁺, Ba²⁺, or Ce⁴⁺ equivalent to the CEC of the saponite. *Clays and Clay Minerals*, 42, 18–22, <https://doi.org/10.1346/CCMN.1994.0420103>.
- Kloprogge, J.T., Komarneni, S., and Amonette, J. (1999) Synthesis of smectite clay minerals: A critical review. *Clays and Clay Minerals*, 47, 529–554, <https://doi.org/10.1346/CCMN.1999.0470501>.
- Komadel, P., Madejová, J., and Bujdak, J. (2005) Preparation and properties of reduced-charge smectites—A review. *Clays and Clay Minerals*, 53, 313–334, <https://doi.org/10.1346/CCMN.2005.0530401>.
- Lanson, B. (2011) Modelling of X-ray diffraction profiles: Investigation of defective lamellar structure crystal chemistry. In M.F. Brigatti and A. Mottana, Eds., *Layered Mineral Structures and Their Application in Advanced Technologies*, Vol. 11, 151–202. Mineralogical Society of Great Britain and Ireland.
- Lee, S. and Xu, H. (2020) Using complementary methods of synchrotron radiation powder diffraction and pair distribution function to refine crystal structures with high quality parameters—A review. *Minerals (Basel)*, 10, 124, <https://doi.org/10.3390/min10020124>.
- Leonardi, A. and Bish, D.L. (2020) Understanding powder X-ray diffraction profiles from layered minerals: The case of kaolinite nanocrystals. *Inorganic Chemistry*, 59, 5357–5367, <https://doi.org/10.1021/acs.inorgchem.9b03464>.
- Leoni, M., Gualtieri, A.F., and Roveri, N. (2004) Simultaneous refinement of structure and microstructure of layered materials. *Journal of Applied Crystallography*, 37, 166–173, <https://doi.org/10.1107/S0021889803022787>.
- Liu, J. and Zhang, G. (2014) Recent advances in synthesis and applications of clay-based photocatalysts: A review. *Physical Chemistry Chemical Physics*, 16, 8178–8192, <https://doi.org/10.1039/C3CP54146K>.
- Madejová, J., Bujdak, J., Gates, W.P., and Komadel, P. (1996) Preparation and infrared spectroscopic characterization of reduced-charge montmorillonite with various Li contents. *Clay Minerals*, 31, 233–241, <https://doi.org/10.1180/claymin.1996.031.2.09>.
- Meunier, A. (2006) Why are clay minerals small? *Clay Minerals*, 41, 551–566, <https://doi.org/10.1180/0009855061420205>.
- Milesi, V.P., Jézéquel, D., Debure, M., Cadeau, P., Guyot, F., Sarazin, G., Claret, F., Vennin, E., Chaduteau, C., Virgone, A., and others. (2019) Formation of magnesium-smectite during lacustrine carbonates early diagenesis: Study case of the volcanic crater lake Dziani Dzaha (Mayotte–Indian Ocean). *Sedimentology*, 66, 983–1001, <https://doi.org/10.1111/sed.12531>.
- Mondillo, N., Nieto, F., and Balassone, G. (2015) Micro- and nano-characterization of Zn-clays in nonsulfide supergene ores of southern Peru. *American Mineralogist*, 100, 2484–2496, <https://doi.org/10.2138/am-2015-5273>.
- Moore, D.M. and Reynolds, R.C. Jr. (1997) *X-ray Diffraction and the Identification and Analysis of Clay Minerals*, 2nd ed., 335–339. Oxford University Press.
- Neder, R.B. and Proffen, T. (2008) *Diffuse Scattering and Defect Structure Simulations: A Cook Book Using the Program DISCUS*, 11096 p. Oxford University Press.
- Newman, A. and Brown, G. (1987) The chemical constitution of clays. In A.C.D. Newman, Ed., *Chemistry of Clays and Clay Minerals*, Mineralogical Society Monograph No. 6. Wiley.
- Ojovan, M.I. and Louzguine-Luzgin, D.V. (2020) Revealing structural changes at glass transition via radial distribution functions. *The Journal of Physical Chemistry B*, 124, 3186–3194, <https://doi.org/10.1021/acs.jpcc.0c00214>.
- Pan, L., Wang, S., Mi, W., Song, J., Zou, J.-J., Wang, L., and Zhang, X. (2014) Undoped ZnO abundant with metal vacancies. *Nano Energy*, 9, 71–79, <https://doi.org/10.1016/j.nanoen.2014.06.029>.
- Perdew, J.P., Burke, K., and Ernzerhof, M. (1996) Generalized gradient approximation made simple. *Physical Review Letters*, 77, 3865–3868, <https://doi.org/10.1103/PhysRevLett.77.3865>.
- Petit, S., Decarreau, A., Mosser, C., Ehret, G., and Grauby, O. (1995) Hydrothermal synthesis (250 °C) of copper-substituted kaolinites. *Clays and Clay Minerals*, 43, 482–494, <https://doi.org/10.1346/CCMN.1995.0430413>.
- Petit, S., Righi, D., and Decarreau, A. (2008) Transformation of synthetic Zn-stevensite to Zn-talc induced by the Hofmann-Klemen effect. *Clays and Clay Minerals*, 56, 645–654, <https://doi.org/10.1346/CCMN.2008.0560605>.
- Ponce, C.P. and Kloprogge, J.T. (2020) Urea-assisted synthesis and characterization of saponite with different octahedral (Mg, Zn, Ni, Co) and tetrahedral metals (Al, Ga, B), a review. *Life*, 10, 168, <https://doi.org/10.3390/10090168>.
- Ross, C.S. (1946) Sauconite—a clay mineral of the montmorillonite Group. *American Mineralogist*, 31, 411–424.
- Schingaro, E., Ventruti, G., Vinci, D., Balassone, G., Mondillo, N., Nieto, F., Lacalamita, M., and Leoni, M. (2021) New insights into the crystal chemistry of sauconite (Zn-smectite) from the Skorpion zinc deposit (Namibia) via a multi-methodological approach. *American Mineralogist*, 106, 290–300, <https://doi.org/10.2138/am-2020-7460>.
- Schlesinger, C., Habermehl, S., and Prill, D. (2021) Structure determination of organic compounds by a fit to the pair distribution function from scratch without prior indexing. *Journal of Applied Crystallography*, 54, 776–786, <https://doi.org/10.1107/S1600576721002569>.
- Smolianinova, N.N., Moleva, V.A., and Organoba, N.I. (1960) New aluminum-free member of the montmorillonite-sauconite series. Academy of Sciences URSS, Commission for Study of Clays, Report to Meeting of International Commission for Study of Clays, 45–52.
- Suquet, H., Malard, C., Copin, E., and Pezerat, H. (1981) Variation du paramètre *b* et de la distance basale *d*₀₀₁ dans une série de saponites à charge croissante: II. Etats 'zero couche.' *Clay Minerals*, 16, 181–193, <https://doi.org/10.1180/claymin.1981.016.2.06>.
- Takahashi, N., Tanaka, M., Satoh, T., Endo, T., and Shimada, M. (1997) Study of synthetic clay minerals. Part IV: Synthesis of microcrystalline stevensite from hydromagnesite and sodium silicate. *Microporous Materials*, 9, 35–42, [https://doi.org/10.1016/S0927-6513\(96\)00084-3](https://doi.org/10.1016/S0927-6513(96)00084-3).
- Tao, Q., Fang, Y., Li, T., Zhang, D., Chen, M., Ji, S., He, H., Komarneni, S., Zhang, H., Dong, Y., and others. (2016) Silylation of saponite with 3-aminopropyltriethoxysilane. *Applied Clay Science*, 132, 133–139, <https://doi.org/10.1016/j.clay.2016.05.026>.
- Tao, Q., Zeng, Q., Chen, M., He, H., and Komarneni, S. (2019) Formation of saponite by hydrothermal alteration of metal oxides: Implication for the rarity of hydrotalcite. *American Mineralogist*, 104, 1156–1164, <https://doi.org/10.2138/am-2019-7043>.
- Treacy, M. M. J., Newsam, J. M., Deem, M. W. (1991) A general recursion method for calculating diffracted intensities from crystals containing planar faults. *Proceedings of the Royal Society of London A: Mathematical*, 433(1889), 499–520.
- Ufer, K., Roth, G., Kleeberg, R., Stanjek, H., Dohrmann, R., and Bergmann, J. (2004) Description of X-ray powder pattern of turbostratically disordered layer structures with a Rietveld compatible approach. *Zeitschrift für Kristallographie - Crystalline Materials*, 219, 519–527, <https://doi.org/10.1524/zkri.219.9.519.44039>.
- Ufer, K., Stanjek, H., Roth, G., Dohrmann, R., Kleeberg, R., and Kaufhold, S. (2008) Quantitative phase analysis of bentonites by the Rietveld method. *Clays and Clay Minerals*, 56, 272–282, <https://doi.org/10.1346/CCMN.2008.0560210>.
- Ufer, K., Kleeberg, R., Bergmann, J., and Dohrmann, R. (2012) Rietveld refinement of disordered illite-smectite mixed-layer structures by a recursive algorithm. II: Powder-pattern refinement and quantitative phase analysis. *Clays and Clay Minerals*, 60, 535–552, <https://doi.org/10.1346/CCMN.2012.0600508>.
- Viani, A., Gualtieri, A.F., and Artioli, G. (2002) The nature of disorder in montmorillonite by simulation of X-ray powder patterns. *American Mineralogist*, 87, 966–975, <https://doi.org/10.2138/am-2002-0720>.
- Vicente, M.A., Suárez, M., López-González, J.D., and Bañares-Muñoz, M.A. (1996) Characterization, surface area, and porosity analyses of the solids obtained by acid leaching of a saponite. *Langmuir*, 12, 566–572, <https://doi.org/10.1021/la950501b>.
- Vogels, R.J.M.J., Kloprogge, J.T., and Geus, J.W. (2005) Synthesis and characterization of saponite clays. *American Mineralogist*, 90, 931–944, <https://doi.org/10.2138/am.2005.1616>.
- Wang, X., Ufer, K., and Kleeberg, R. (2018) Routine investigation of structural parameters of dioctahedral smectites by the Rietveld method. *Applied Clay Science*, 163, 257–264, <https://doi.org/10.1016/j.clay.2018.07.011>.
- Wang, L., Bahnmann, D.W., Bian, L., Dong, G., Zhao, J., and Wang, C. (2019) Two-dimensional layered zinc silicate nanosheets with excellent photocatalytic performance for organic pollutant degradation and CO₂ conversion. *Angewandte Chemie International Edition*, 58, 8103–8108, <https://doi.org/10.1002/anie.201903027>.
- Yang, D. and Frindt, R.F. (1996) Powder X-ray diffraction of turbostratically stacked layer systems. *Journal of Materials Research*, 11, 1733–1738, <https://doi.org/10.1557/JMR.1996.0217>.
- Young, C.A. and Goodwin, A.L. (2011) Applications of pair distribution function methods to contemporary problems in materials chemistry. *Journal of Materials Chemistry*, 21, 6464–6476, <https://doi.org/10.1039/c0jm04415f>.
- Zhou, R., Basu, K., Hartman, H., Matocha, C.J., Sears, S.K., Vali, H., and Guzman, M.I. (2017) Catalyzed synthesis of zinc clays by prebiotic central metabolites. *Scientific Reports*, 7, 533, <https://doi.org/10.1038/s41598-017-00558-1>.

MANUSCRIPT RECEIVED MAY 13, 2022

MANUSCRIPT ACCEPTED AUGUST 12, 2022

ACCEPTED MANUSCRIPT ONLINE AUGUST 24, 2022

MANUSCRIPT HANDLED BY HONGWU XU

Endnote:

¹Deposit item AM-23-78591, Online Materials. Deposit items are free to all readers and found on the MSA website, via the specific issue's Table of Contents (go to http://www.minsocam.org/MSA/AmMin/TOC/2023/Jul2023_data/Jul2023_data.html). The CIF has been peer-reviewed by our Technical Editors.